

In-situ Modification of a High Entropy Alloy With 2.4% Molybdenum Using LPBF, and its Effect on Microstructure and Corrosion Resistance

M. Ritchie*, S. Mehraban, S. G. R. Brown, D. Butcher, J. Cullen, M. Calvo-Dahlborg and N.
P. Lavery

Abstract

Laser powder bed fusion (LPBF) components display higher porosity compared to parts made by conventional processes and these pores act as preferential initiation sites for pitting corrosion to occur. In stainless steels such as 316L, molybdenum is 3.5X more effective at enhancing the pitting resistance than chromium, without adding unwanted nitrides to the alloy. In this work, the effect on corrosion resistance is reported for an Al-Cr-Mn-Ni-Fe high entropy alloy (HEA) gas atomised specifically for LPBF, as well as the effects of modifying the alloy by blending the HEA with molybdenum. In-situ LPBF processing, even for low levels of additions has made the comparison difficult, as the pitting resistance is so strongly linked to the porosity, which is higher in the in-situ process. Pitting resistance for both the original HEA and the doped HEA will be compared between samples processed by casting and by LPBF.

Keywords: High Entropy Alloy, Laser Powder Bed Fusion, Pitting Corrosion.

Introduction

The LPBF process continues to grow as an important additive manufacturing (AM) process for a diverse set of critical applications where high density is required. Porosity occurring from the LPBF process has been shown to reduce the mechanical properties of metals, from tensile strength and elastic modulus to elongation [1–4]. This is particularly relevant in aerospace and automotive industries where failure in critical components could result in loss of life. Aerospace manufacturing is therefore subject to extensive quality control, a hurdle for the AM industry as many studies report disparities in mechanical properties due to the many parametrical influences on component quality [3,5–7]. Unlike other ways of manufacturing net-shape parts, LPBF offers much greater design freedom, with an increasing palette of alloys, mostly based on traditional alloys used in specific applications [8,9]. These alloys were developed a long time ago for other processing routes such as casting such as AlSi10 and AlSi7 or forging with Ti-6Al-4V, where the cooling rates are much lower than LPBF. Even when traditional alloys can be used, the high cooling rates result in heterogeneous microstructures with long columnar grains, leading to different mechanical properties to what might be expected, such as higher hardness at the expense of lower ductility [10,11]. An added consideration is the porosity levels, which although increasingly low in new generations of machines, still affects properties such as corrosion and fatigue strength, with surface pores operating as preferential sites for pitting corrosion [12,13]. However, not all alloys can be successfully used in LPBF, and those with poor weldability such as Ni based alloys like Hastelloy X often having the narrowest process operating windows making it difficult to make parts without defects, namely porosity and/or solidification cracking [14].

H13 is a good example of an alloy which is difficult to process by LPBF. As a steel used in tooling such as injection moulding it is expected to have good thermal fatigue strength and an acceptable level of corrosion resistance. H13 is currently being modified to process better, both during LPBF and after building, with integrated heat treatments [15–17]. Because of this, there is an increasing body of work going into deriving AM specific alloys (e.g. Scalmetal aluminium alloy), or modified traditional alloys (e.g. H13) [18,19]. However, there

are still many areas where more work needs to be done such as alternatives to high grade aluminium alloys.

HEAs are generally accepted to be a system of 5 or more principal elements, the concentrations of which fall between 5 and 35at.% [20–22]. This differs from the standard makeup of stainless steels for example, which use Fe to make up the bulk of the composition, with additional elements added in smaller quantities to provide preferential characteristics. The compositions of HEAs can be equimolar or not, either way, the vast number of possible combinations is one of the main reasons for the interest in the field along with the simplicity of their design and the ability to tailor constituent elements to achieve desired characteristics [20]. The majority of HEA creation has occurred in arc melters or induction coils, and LPBF is only just being researched as an alternative manufacturing method. HEA production can be a complex process with high levels of control required to manufacture them. Therefore, the parameter control and fast cooling rates generated by LPBF suggests that the process could be suitable replacement to create components from HEAs [20]. Work on HEAs processed by laser cladding and LPBF is increasingly being published, but this method of production is still in its infancy [20,23].

The pitting resistance equivalent number (PREN) is used to predict a stainless steels resistance to pitting corrosion, with it equating to the $\text{wt.\%Cr} + 3.3 \times \text{wt.\%Mo} + 16 \times \text{wt.\%N}$. The addition of 2.4% Mo to the HEA in this paper was based on its theoretically larger influence on the pitting resistance than Cr [24,25].

Materials and Methodology

The 316L and HEA1 analysis and corrosion specimens were produced from virgin 15 μm - 45 μm powder provided by Sandvik in a Renishaw AM400 machine on full sized build plates after running parameter optimisations studies. To create the HEA1 + 2.4% Mo mixture, 122.951g of powdered Mo (<5 μm) was added to 5Kg of HEA1, and put into a LFA V-type blender for 2 hours at an agitation speed of 60r/min to allow for homogenous distribution of the Mo. Compositional analysis was undertaken on the resultant blend to confirm the target levels of Mo had been reached before it was loaded into a reduced build volume (RBV) within the AM 400 to produce samples for analysis and corrosion using parameters based on those used for HEA1. Table 1 shows the target and achieved compositions of the blended mixture with Figure 1 showing SEM images of the powder at 550x (a) and 1100x (b) magnification. HEA1 particles appear much larger due to the size of the particles used.

Table 1. Target and achieved compositions for HEA1 and HEA1 + 2.4% Mo (all in wt.%)

	Fe	Cr	Ni	Mn	Al	N	Si	C	Mo
HEA1 (Measured)	33.97	27.3	25	10.3	2.8	0.20	0.4	0.02	-
Target HEA1+2.4 Mo	33.15	26.64	24.40	10.05	2.73	0.20	0.39	0.02	2.4
Achieved HEA1+2.4 Mo	31.45	26.39	25.36	10.46	3.20	0.24	0.54	0.03	2.33

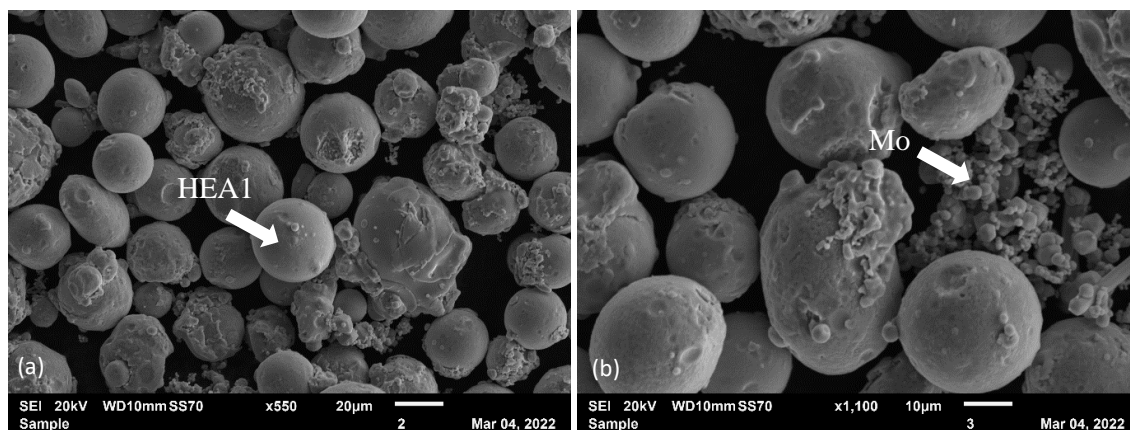


Figure 1. HEA1 + 2.4% Mo at 550x (a) and 1100x (b) magnification

Cast samples were created from a combination of feedstock and weighed approximately 40g. These feedstocks were re-melt samples produced through LPBF, or powder weighed out and compacted using a Baileigh hydraulic press. All the feedstock produced stemmed from the same 15µm - 45µm powder referenced previously, as did the Mo. The feedstock was melted under argon (>99.9% pure) in an induction heater in 15mm diameter crucibles. Once molten, the 316L was held at temperature for 1 minute whilst the HEA samples held for 5. The extra duration for the HEAs was to allow the elements to diffuse uniformly through the sample. Two samples of each alloy were produced, one to section for compositional, microstructural, and porosity analysis, and another for corrosion testing.

All samples for analysis were subjected to a 5-stage grinding and polishing regime, resulting in a 1µm finish. Porosity analysis was conducted on AM samples using a Biolin Scientific Sigma 700 force tensiometer and Archimedes calculations. All samples were then imaged using a Zeiss Observer inverted light microscope, with its stitching function used to map the full sample area. The images were put through ImageJ to analyse the porosity and in the case of the AM samples, compare this data to that obtained from the tensiometer. Microstructure and compositional analysis were performed on a JEOL JSM-6010 Secondary Electron Microscope with Energy Dispersive X-ray Spectrometry SEM-EDS. EDS maps were used to verify the bulk chemistry with the target chemistries with point analysis used to acquire the compositions of different phases within the microstructure. All SEM and EDS images used are taken of horizontal slices, in the case of the AM samples, these were perpendicular to the build direction.

Corrosion specimens of approximately 1.5mm thickness were cut from the AM and cast samples, soldered to electrical wiring and subsequently cold mounted. These were then polished as previously discussed. Once complete, they were exposed to an open circuit potential (OCP) scan and a cyclic polarisation test, with multiple tests were carried out per sample.

Results

Microstructure Analysis

Figure 2 shows the cast microstructures of HEA1 (a) and HEA1 + 2.4% Mo (b). These images show that initially HEA1 has two dominant phases, and the addition of the Mo creating

a third. Thermocalc predicts that the lighter phase in HEA1 is FCC_L12, with the darker region being BCC_B2.

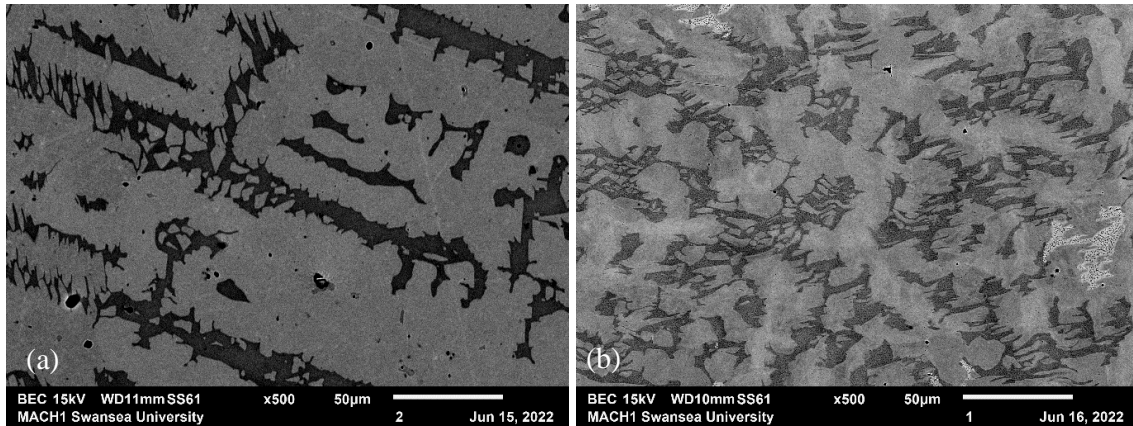


Figure 2. Cast microstructure of HEA1 (a) and HEA1 + 2.4% Mo (b)

The EDS mapping of HEA1 in Figure 3 shows a high Cr level present in the darker BCC phase, which coincides with a lower Ni reading. The inverse is true in the lighter FCC phase, with the Ni being comparatively higher than the BCC phase and Cr levels dropping. Point scans of each phase confirm this observation, with the Cr and Ni rich phase readings being 12.98wt.% and 13.04wt.% higher respectively than their depleted counterparts. These readings are similar to those predicted by Thermocalc.

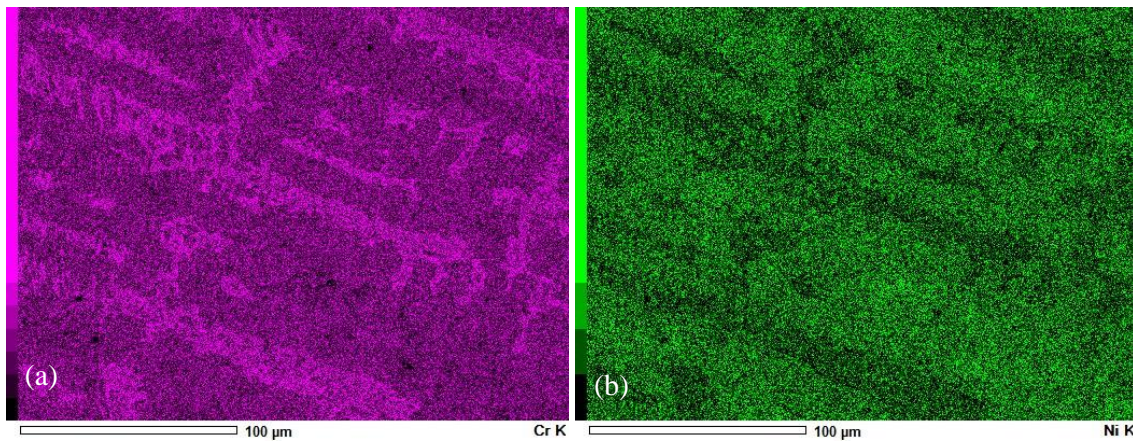


Figure 3. Cr (a) and Ni (b) EDS maps for cast HEA1

As with HEA1, the EDS analysis of HEA1 + 2.4% Mo in Figure 4 shows Cr abundance and Ni depletion and in the BCC phase, with the inverse true in the FCC phase. The addition of Mo does not appear to have affected this relationship, with the EDS map of Mo suggesting a similar phase relationship to Cr, with a greater abundance in the BCC phase compared to the FCC. The third phase not apparent in HEA1 appears to be another that is richer in Cr and Mo and depleted of Ni. Again, point scans of these areas confirm this prediction, with an even larger compositional differential between the phases when compared to HEA1 observed. Analysis shows a 15.94wt.% and 2.15wt.% increase in Cr and Mo levels respectively in the BCC phase compared to the FCC. Conversely, Ni is observed at 15.81wt.% higher in the FCC phase compared to the BCC. The elements in the third phase occur at levels similar to those in the BCC with the other elements remaining relatively constant between each phase.

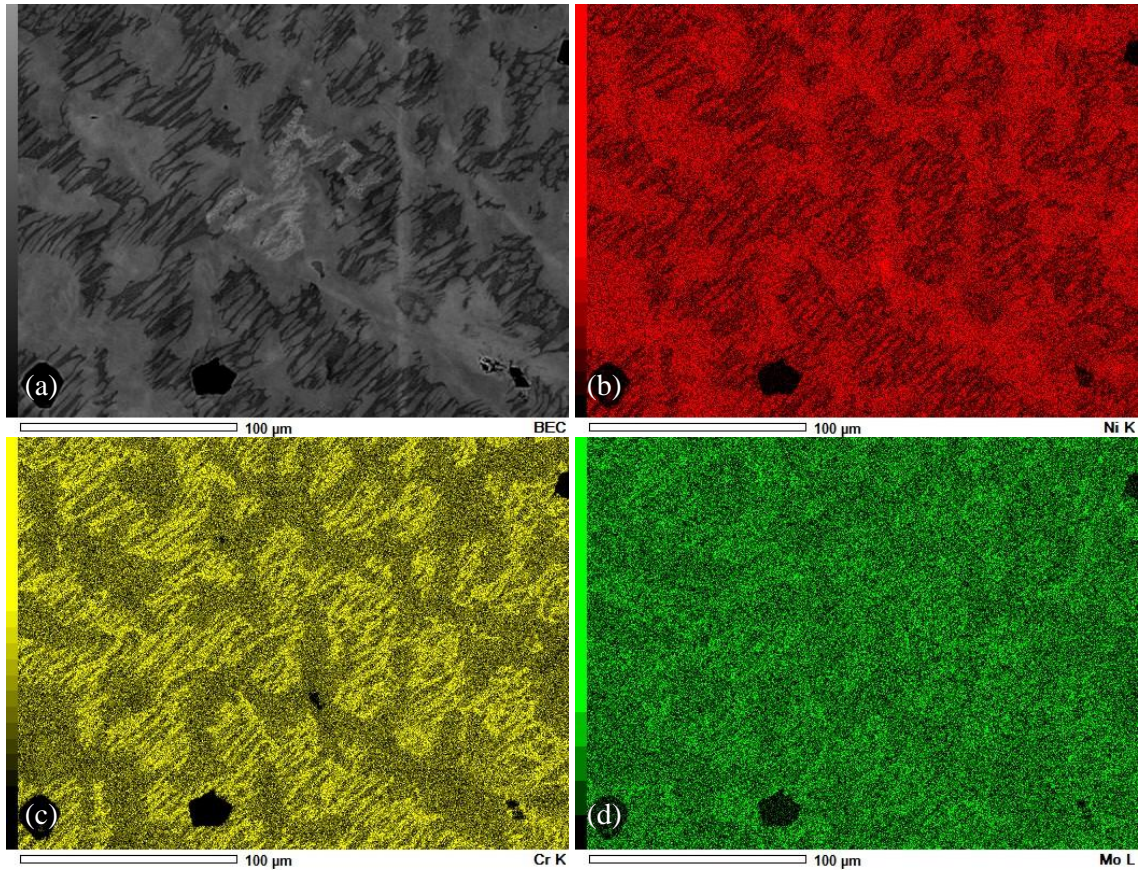


Figure 4. Cast microstructure (a) and EDS maps of Ni (b), Cr (c), and Mo (d) for HEA1 + 2.4% Mo

Figure 5 shows the AM microstructures of HEA1 (a) and HEA1 + 2.4% Mo (b). Comparing these to the microstructures seen from the cast specimens of the same alloys in Figure 2, the dendritic structure looks to have disappeared at 500x magnification, leaving behind more defined grain boundaries. The white spots seen in (b) are likely due to charging from the electron beam.

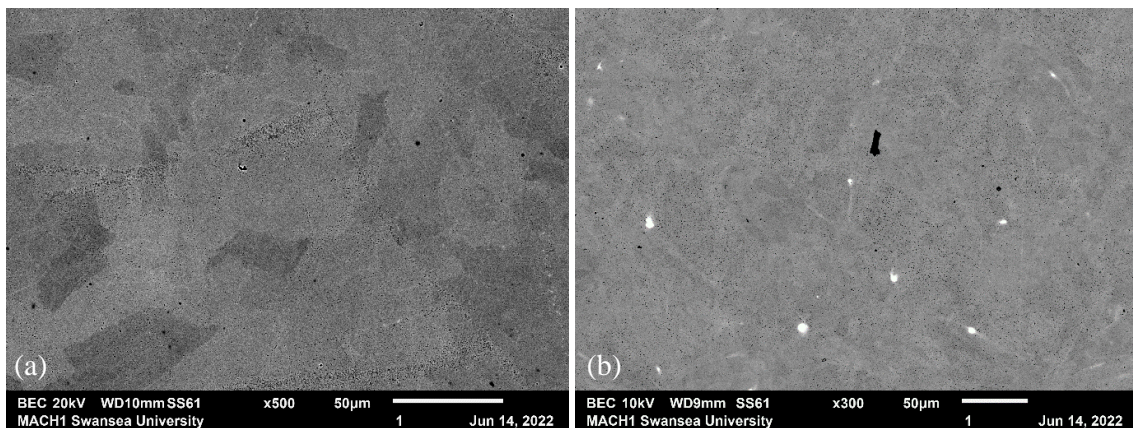


Figure 5. Microstructure of AM HEA1 (a) and HEA1 + 2.4% Mo (b)

Similar to the cast microstructures, different phases appear to occur in the microstructure, however, EDS mapping and point scans show that these different regions are compositionally comparable, with a maximum elemental deviation of 0.28wt.% between each region. EDS maps of Cr and Ni are where this is seen most prominently as shown in Figure 6. When compared to their cast counterparts in Figures 3 and 4, there are no distinct areas of richness, depletion, or segregation as there were in the cast samples.

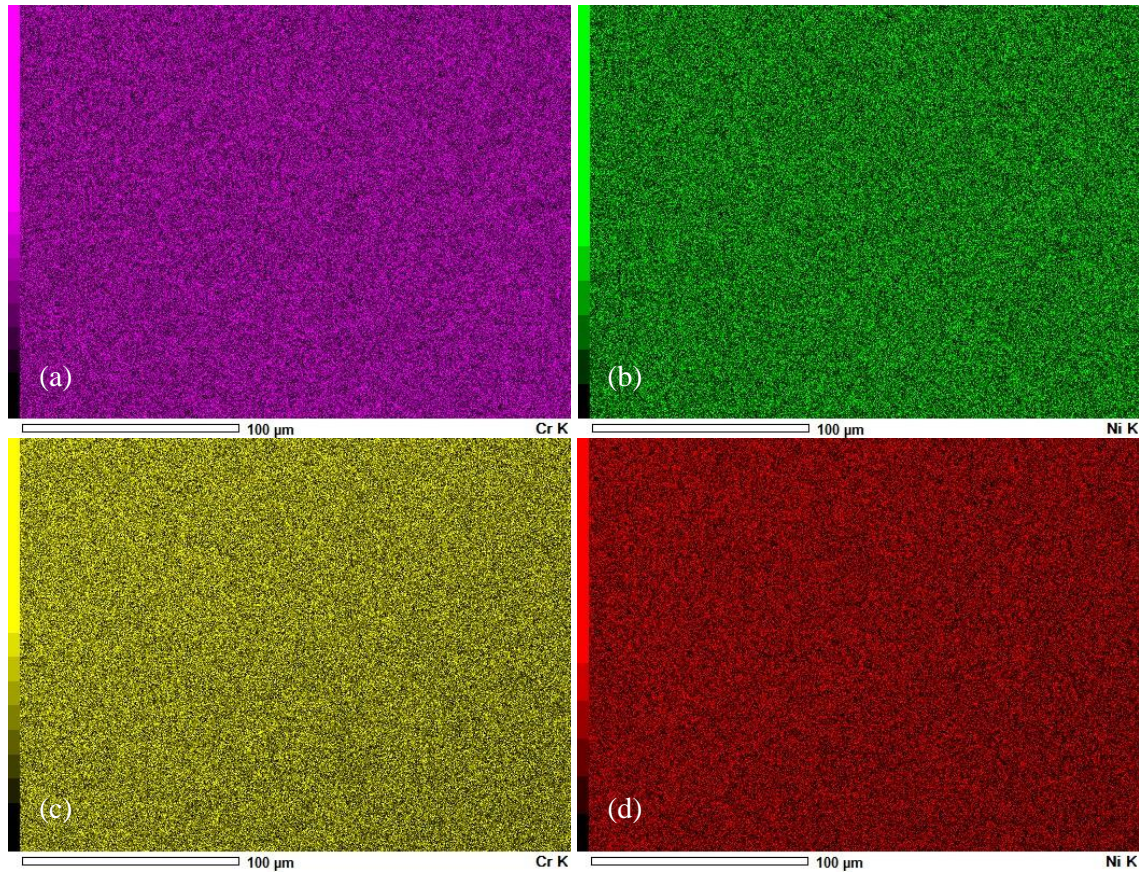


Figure 6. EDS maps of Cr and Ni for AM HEA1 (a,b) and HEA1 + 2.4% Mo (c,d)

Corrosion Analysis

Figure 7 shows the result of cyclic polarisation scans on cast and AM samples of 316L, HEA1 and HEA1 + 2.4% Mo. First observations show that, whilst the 316L test specimens have a clear pitting potential (E_{pit}), the HEA alloys corrode at a steadier rate with a much less obvious E_{pit} . Other graphed aspects between 316L and the HEAs can also be compared, such as the metastable pitting phase that occurs after the corrosion potential (E_{corr}) is reached. With 316L, the current measured remains fairly consistent as the voltage applied continues to increase, until the E_{pit} is reached. The HEAs current however consistently increases, with only minor evidence of any metastable pitting. Key data from these graphs has been extracted and is displayed in Table 2.

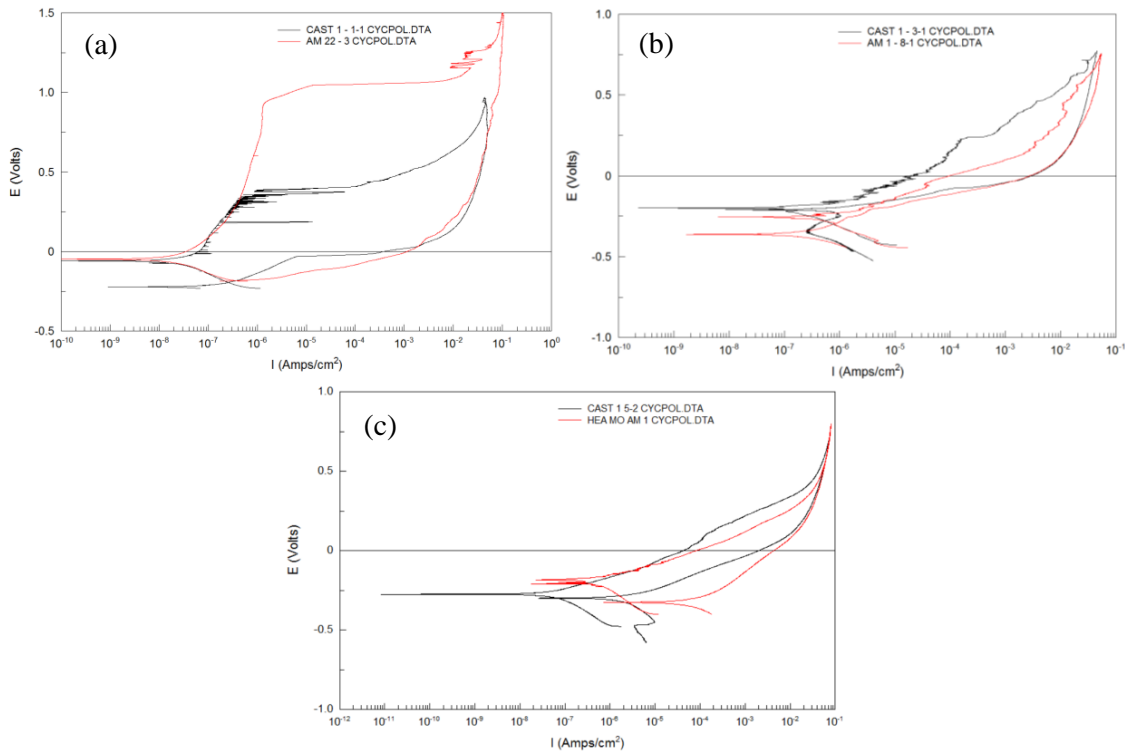


Figure 7. Cyclic polarisation graphs for cast and AM samples of 316L (a), HEA1 (b), and HEA1 + 2.4% Mo (c)

Table 2. Corrosion data extracted from Figure 7

	E_{corr} (V)	E_{pit} (V)	$E_{pit} - E_{corr}$ (V)	Re-passivation potential (V)
316L Cast	-0.058	0.376	0.434	-0.191
316L AM	-0.047	0.927	0.974	-0.183
HEA1 Cast	-0.199	0.231	0.430	-0.208
HEA1 AM	-0.254	-0.047	0.207	-0.294
HEA1 + 2.4% Mo Cast	-0.274	0.100	0.374	-0.298
HEA1 + 2.4% Mo AM	-0.208	0.159	0.367	-0.324

Discussion

The differences in microstructure observed between the AM and cast samples imaged, as well as the differences in phase formation and elemental segregation are often attributed to the rapid rate at which the AM process heats and cools the part. The HEA castings were held at molten for 5 minutes to allow for full diffusion of the elements within the alloy, and the cooling happens over a number of minutes. The AM process conducts the fusion of an entire layer of a density cube within a second, with the heat created being rapidly dissipated through the adjacent, unmelted powder and the baseplate. This facilitates minimal diffusion and subsequently, no areas of rich and depleted elemental abundance like that which is seen in the cast samples.

The addition of 2.4wt.% Mo to HEA1 does appear to have added a third clear phase to the microstructure, although further work with ThermoCalc and X-ray diffraction (XRD) is

needed to confirm the details of this phase, and why the Mo appears to migrate towards the Cr rich regions. Along with this third phase, the phases in HEA1 + 2.4% Mo appear to be more irregular than those in HEA1. The phases of HEA1 are observed to form parallel or perpendicular to each other, whereas there is more of a branch-like structure with the Mo addition. This, however, could be due to processing, as every cast is different, so further repeats and analysis would be required to verify whether it is in fact a characteristic induced by the addition, or simply variations in the manufacturing process.

HEA1 + 2.4% Mo built in the RBV was more difficult to process than anticipated, but this could be down to multiple factors. Mo has a melting point of over 2600°C, compared to the alloyed HEA1 which is below 1800°C. The Mo powder was also not manufactured specifically for AM, and with its particle size being <5µm and with that of HEA1 being between 15µm - 45µm, the Mo could have increased the packing density, and therefore the amount of energy required per mm³. These combined suggest increasing the energy density when processing the alloy through AM could overcome the melting point differential, and any issues caused by the packing density. Also, due to the sphericity of the particles not being a target for the Mo in production, the subsequent lack of could decrease the flowability of the overall material when distributed by the wiper blade, leading to problems caused by an uneven supply.

The corrosion of the HEAs appear to translate well between the different manufacturing processes when compared to that of 316L, which has a larger differential. In the regions between E_{corr} and E_{pit} for the HEAs and 316L, clear metastable pitting occurs in 316L along with minimal change in current, but with both HEAs, the current continues to increase in line with the voltage, with only marginal signs of the metastable phase. The metastable phase occurs due to the formation of a passive film on the surface of the metal, protecting the corrosion site from further attack. All the alloys have Cr present in similar quantities which is one of the elements responsible for the generation of the passive layer, however it appears more effective during that stage of the corrosion cycle in 316L than the HEAs. Having said this, the $E_{\text{pit}} - E_{\text{corr}}$ for the three cast samples shown in Table 2 do not differ significantly, ranging from 0.434V for 316L to 0.374V for HEA1 + 2.4% Mo.

The Mo addition to HEA1 does not appear to have had the desired effect when comparing the cast specimens, with the $E_{\text{pit}} - E_{\text{corr}}$ actually decreasing by 0.056V. This could be due to the greater disparity between the Cr rich BCC phase and its depleted FCC phase, increasing from 12.98% in HEA1 to 15.94% in HEA1 + 2.4% Mo. With the Mo segregation also following this trend there are regions of the microstructure that have a significantly lower abundance of the elements associated with corrosion resistance. These depleted regions could therefore be acting as a preferential site for corrosion to occur. Conversely, when the addition is processed through the AM route, it does seem to have a preferential effect on the corrosion resistance, with the $E_{\text{pit}} - E_{\text{corr}}$ rising by 0.160V. The EDS analysis of the AM specimens showed a much more homogenous elemental distribution, and therefore no regions that would act as a preferential site of corrosion when compared to the cast samples in the same fashion. This could explain why the Mo addition benefits the corrosion resistance in the AM sample, whilst not being seen in that of the cast.

Conclusion

To conclude, the microstructural changes by adding Mo to HEA1, including the third phase formation and the migration of Mo to the Cr rich phases in the cast specimens needs to

be understood to a greater extent, as well as its effect on the corrosion performance. This is less relevant in the AM specimens where no significant depletion occurs in any of the grains or phases. The corrosion data extracted from the cyclic polarisation scans for the HEAs suggests a varying effect of the Mo addition on their pitting resistance that is dependent on their manufacturing method. However, the irregular nature of cast and AM surfaces necessitates further analysis on HEA1 and HEA1 +2.4% Mo to determine the effectiveness of the Mo addition at increasing the corrosion resistance of HEA1.

- [1] Kan WH, Chiu LNS, Lim CVS, Zhu Y, Tian Y, Jiang D, et al. A critical review on the effects of process-induced porosity on the mechanical properties of alloys fabricated by laser powder bed fusion. *J Mater Sci [Internet]*. 2022;57(21):9818–65. Available from: <https://doi.org/10.1007/s10853-022-06990-7>
- [2] du Plessis A, Yadroitsava I, Yadroitsev I. Effects of defects on mechanical properties in metal additive manufacturing: A review focusing on X-ray tomography insights. *Mater Des*. 2020 Feb 1;187:108385.
- [3] Lewandowski JJ, Seifi M. Metal additive manufacturing: A review of mechanical properties (postprint). 2016;
- [4] Frazier WE. Metal additive manufacturing: a review. *J Mater Eng Perform*. 2014;23(6):1917–28.
- [5] Seifi M, Gorelik M, Waller J, Hrabec N, Shamsaei N, Daniewicz S, et al. Progress Towards Metal Additive Manufacturing Standardization to Support Qualification and Certification. *JOM*. 2017 Mar 1;69(3):439–55.
- [6] Seifi M, Salem A, Beuth J, Harrysson O, Lewandowski JJ. Overview of Materials Qualification Needs for Metal Additive Manufacturing. *JOM*. 2016 Mar 1;68(3):747–64.
- [7] Li P, Warner DH, Fatemi A, Phan N. Critical assessment of the fatigue performance of additively manufactured Ti-6Al-4V and perspective for future research. *Int J Fatigue*. 2016 Apr 1;85:130–43.
- [8] Gibson I, Rosen D, Stucker B, Khorasani M. Additive Manufacturing Technologies. *Additive Manufacturing Technologies*. 2021.
- [9] Wohlers T, Gornet T. History of Additive Manufacturing 2014. *Wohlers Rep 2014 - 3D Print Addit Manuf State Ind*. 2014;
- [10] Shakil SI, Hadadzadeh A, Shalchi Amirhiz B, Pirgazi H, Mohammadi M, Haghshenas M. Additive manufactured versus cast AlSi10Mg alloy: Microstructure and micromechanics. *Results Mater*. 2021 Jun 1;10:100178.
- [11] Read N, Wang W, Essa K, Attallah MM. Selective laser melting of AlSi10Mg alloy: Process optimisation and mechanical properties development. *Mater Des*. 2015 Jan 1;65:417–24.
- [12] Trelewicz JR, Halada GP, Donaldson OK, Manogharan G. Microstructure and Corrosion Resistance of Laser Additively Manufactured 316L Stainless Steel. *JOM*. 2016;68(3).
- [13] Sander G, Thomas S, Cruz V, Jurg M, Birbilis N, Gao X, et al. On The Corrosion and Metastable Pitting Characteristics of 316L Stainless Steel Produced by Selective Laser Melting. *J Electrochem Soc*. 2017;164(6).
- [14] Muhammad M, Ghiaasiaan R, Gradl PR, Schobel A, Godfrey D, Shao S, et al. Additively Manufactured Hastelloy-X: Effect of Post-Process Heat Treatment on Microstructure and Mechanical Properties. In: *2021 International Solid Freeform Fabrication Symposium*. University of Texas at Austin; 2021.
- [15] Mertens R, Vrancken B, Holmstock N, Kinds Y, Kruth JP, Van Humbeeck J. Influence of powder bed preheating on microstructure and mechanical properties of H13 tool

- steel SLM parts. *Phys Procedia*. 2016;83:882–90.
- [16] Wang L zhi, Wu J jiao, Huang X fei, Hong X fu. SLM-manufactured 30CrMnSiA alloy: Mechanical properties and microstructural effects of designed heat treatment. *Opt Laser Technol*. 2018 Nov 1;107:89–98.
- [17] Lee J, Choe J, Park J, Yu JH, Kim S, Jung ID, et al. Microstructural effects on the tensile and fracture behavior of selective laser melted H13 tool steel under varying conditions. *Mater Charact*. 2019 Sep 1;155.
- [18] Yuan M, Cao Y, Karamchedu S, Hosseini S, Yao Y, Berglund J, et al. Characteristics of a modified H13 hot-work tool steel fabricated by means of laser beam powder bed fusion. *Mater Sci Eng A*. 2022 Jan 13;831:142322.
- [19] Schmidtke K, Palm F, Hawkins A, Emmelmann C. Process and Mechanical Properties: Applicability of a Scandium modified Al-alloy for Laser Additive Manufacturing. *Phys Procedia*. 2011 Jan 1;12(PART 1):369–74.
- [20] Brif Y, Thomas M, Todd I. The use of high-entropy alloys in additive manufacturing. *Scr Mater* [Internet]. 2015;99:93–6. Available from: <http://dx.doi.org/10.1016/j.scriptamat.2014.11.037>
- [21] Cantor B, Chang ITH, Knight P, Vincent AJB. Microstructural development in equiatomic multicomponent alloys. *Mater Sci Eng A*. 2004 Jul 1;375–377(1-2 SPEC. ISS.):213–8.
- [22] Chen TK, Shun TT, Yeh JW, Wong MS. Nanostructured nitride films of multi-element high-entropy alloys by reactive DC sputtering. *Surf Coatings Technol*. 2004 Nov 1;188–189(1-3 SPEC.ISS.):193–200.
- [23] Kuncic I, Polanski M, Bystrzycki J. Structure and hydrogen storage properties of a high entropy ZrTiVCrFeNi alloy synthesized using Laser Engineered Net Shaping (LENS). *Int J Hydrogen Energy* [Internet]. 2013;38(27):12180–9. Available from: <http://dx.doi.org/10.1016/j.ijhydene.2013.05.071>
- [24] Deme M. Pitting Corrosion of Type 316L Stainless Steel Elaborated by the Selective Laser Melting Method : Influence of Microstructure. 2021;30(July):5050–8.
- [25] Köhler ML, Kunz J, Herzog S, Kaletsch A, Broeckmann C. Microstructure analysis of novel LPBF-processed duplex stainless steels correlated to their mechanical and corrosion properties. *Mater Sci Eng A*. 2021 Jan 13;801:140432.